This article has been accepted for publication in a future issue of this journal, but has not been fully edited. Content may change prior to final publication.
DOI: 10.17775/CSEEJPES.2023.00110

Grid Forming $\mathcal{H}_\infty$ control for HVDC Diode Rectifier-connected Wind Power Plants

Jaime Martínez-Turégano, Antonio Sala, and Ramon Blasco-Gimenez

***Abstract*—Grid forming controllers need to operate with a large variation of grid parameters and grid structure, for instance, during black-start operation, connection to HVDC diode rectifiers, etc. This paper proposes a methodology for the synthesis of robust grid forming controllers for HVDC Diode Rectifier based Wind Power Plants using $\mathcal{H}_\infty$ control. The different operating modes of a HVDC Diode Rectifier based Wind Power Plant are be considered for the controller synthesis using the proposed $\mathcal{H}_\infty$ controller design methodology. The proposed methodology for grid forming controller design improves the performance and robustness of well tuned standard proportional-resonant based controllers. The results have been validated experimentally at the wind turbine level by means of a small power prototype. The validation at the system level has been carried out using a realistic simulation of a HVDC Diode Rectifier-connected Wind Power Plant.**

***Index Terms*—Grid forming, $\mathcal{H}_\infty$ controller, Diode Rectifier, HVDC, Wind Power Plants**

I. Introduction

THE use of Diode Rectifiers (DRs) is an alternative for the HVDC connection of off-shore Wind Power Plants (WPP) to the on-shore grid. As DRs are passive converters, the WPP requires grid forming capability for its operation.

Different authors have proposed HVDC DR stations as a technical solution that significantly reduces the cost of off-shore infrastructure while increasing the overall efficiency and robustness of the entire system [1], [2], [3]. Siemens estimates that the use of HVDC DR stations could reduce the WPP connection cost up to 30%, mainly due to the use of less expensive devices, highly reduced footprint and the corresponding important savings on platform costs [4], [5], [6]. Additionally, the diode based rectifier has smaller losses than any other high power HVDC rectifier [7].

Furthermore, several control alternatives have been proposed for DR based WPPs in order to provide grid forming capability. Authors in [8] propose a technique for the distributed voltage and frequency control of the local ac-grid in off- shore WPP based on type-4 grid forming wind turbines. In [9], a distributed phase-locked loop-based frequency control is proposed for the same purpose.

Considered DR-connected wind power plants have different modes of operations, islanding at no-load (ISL), supply of loads during ISL (ISL-full/partial load), or power transmission through the DR-HVDC link (DR-connected). Clearly, the grid characteristics in these kind of systems change widely depending on the different operating modes, power levels and off-shore grid structure (e.g. number of strings connected). Therefore, Wind Turbine Generators (WTGs) see widely changing impedances in each operating mode, which could lead to poor controller performance or even to instability. Previous research on DR-grid forming control did not address this important issue [10], [11], [12].

This paper will consider the use of $\mathcal{H}_\infty$ synthesis techniques [13], [14] for the development of robust grid forming voltage controllers for DR-connected WPPs, as this tool provides an optimal controller for a given set of frequency weights that take into account plant and measurement uncertainties in different frequency ranges. The design in $\alpha\beta$ frame is preferred in this paper so a linear voltage controller is used for a linear plant, thus avoiding non-linearities and approximations arising from the use of a positive sequence dq frame control. Moreover, an $\alpha\beta$ resonant controller would provide both positive and negative sequence voltage control [15].

$\mathcal{H}_\infty$ synthesis has been previously used for Voltage Source Converter (VSC) control [16], [17]. However, previous work did not consider $\alpha\beta$ frame design for grid forming converters, nor studied its application to DR-connected WPPs.

Authors of [18] proposed a $\mathcal{H}_\infty$ synthesis for the current control loop of grid following converters in a stationary $\alpha\beta$ frame models. Similarly, authors of [19] used $\mathcal{H}_\infty$ techniques for a systematic design of robust and optimal grid following converters. In both cases, the application to grid forming converters was not addressed. $\mathcal{H}_\infty$ fixed structure synthesis is used in [20] to tune the gain values of a grid forming converter with droop, voltage and current loops. This methodology does not consider how the system impedance can change for the different operating modes, nor is valid for control design based on $\alpha\beta$ frame. Authors in [21] propose to combine a sliding mode current control with a PI-based voltage control tuned using $\mathcal{H}_\infty$ synthesis to be able to use models with reduced accuracy during controller design. In any case, the different modes of operation are not considered for the controller design. In [22], single voltage control and cascade voltage and current control is considered for a $\mathcal{H}_\infty$ controller design based on passivity. However, voltage and current control loops are independently designed, leading to a sub-optimal result and robustness to grid impedance changes is not explicitly considered. Moreover, the resonant behaviour of the controller is achieved including a external resonator to the controller and not as a result of the synthesis procedure.

Authors would like to acknowledge the support of the Spanish Research Agency through grant PID2020-112943RB-I00 funded by MCIN/AEI/10.13039/501100011033 and grant PDC2021-121077-I00 funded by MCIN/AEI/10.13039/501100011033 and by the European Union NextGenerationEU/PRTR.

Jaime Martínez-Turégano, Antonio Sala, and Ramon Blasco-Gimenez are with the Universitat Politècnica de València, 46022 València, Spain.

To the authors' knowledge, this is the first work that uses $\mathcal{H}_\infty$ based design to consider the different operational modes for the design DR connected WTG grid forming voltage controllers, ensuring system stability, while providing the desired dynamic performance.

The proposed controller is validated experimentally at the WTG level using a small power prototype, so converter non-linearities and DSP implementation effects are not overlooked. Then, a detailed simulation of a large scale WPP is used to validate the controller in a realistic scenario, including a large number of WTGs, non-linear transformers and cables and with a low grid damping characteristic of large power systems.

Results show that the proposed $\mathcal{H}_\infty$ based control design methodology achieves better performance, robustness and harmonic rejection than using well-tuned PR based controllers for the different operating modes of a DR-connected WPP.

This paper is structured as follows. The second section describes the HVDC diode rectifier connected off-shore WPP system, which will be used as a realistic scenario. The third section describes the proposed $\mathcal{H}_\infty$ based controller design methodology for the grid side converter of a grid forming WTG. The following section shows the results of the designed controllers in lab scale WTG converter prototype and a study in a realistic scenario based on detailed simulations. The last section of this paper includes the discussions and conclusions.

II. System Description and Problem Statement

This section describes the DR based off-shore WPP that has been considered in order to analyse the designed controllers.

Fig. 1 shows the diagram of the entire system, consisting of a 1200 MW off-shore WPP distributed in three clusters of 400 MW each. The WPP is connected via a DR-HVDC link to a full-bridge on-shore Modular Multi-level Converter (MMC).

Each WPP cluster is composed of fifty 8 MW rated WTGs. Each cluster is modelled as a detailed string and a number of aggregated strings, as shown in Fig. 1. The WTG aggregation technique used is the one proposed in [23]. Moreover, each WPP cluster WPP-i ($i = 1, 2, 3$) is connected to the corresponding DR platform through the off-shore ac-grid. All ac-cables considered for the off-shore ac-system are modelled using lumped π-parameters.

The system includes three DR platforms [4]. Every platform consists of two 12-pulse DR of 200 MW each one that are connected in parallel on the ac-side and in series in their dc-side. Additionally, ac and dc filters are placed in each DR platform. The HVDC export cable is modelled considering distributed frequency dependent parameters.

A. System Modelling

The dynamics of the LC filter plus the WTG transformer in Fig. 1 are:

$$V_W = R_W I_W + L_W \frac{dI_W}{dt} + V_C \tag{1}$$

$$I_W - I_T = C_W \frac{dV_C}{dt} \tag{2}$$

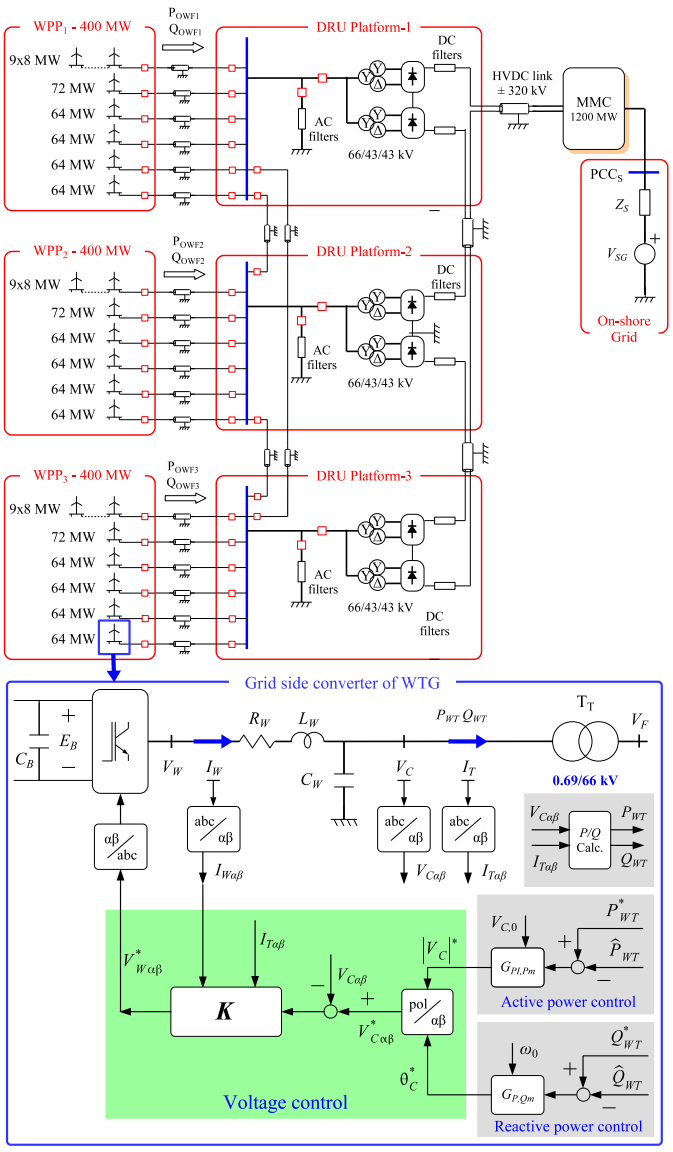

Fig. 1. WPPs connected to the on-shore ac-grid via a diode-based HVDC link

$$V_C = R_T I_T + L_T \frac{dI_T}{dt} + V_F \tag{3}$$

where V_W is the output converter voltage, I_W is the output converter current, V_C is the capacitor C_W voltage, I_T is the current through the transformer T_T, and V_F is the voltage at the output of the transformer T_T. The parameters of the L-C filter are L_W, R_W and C_W, and L_T and R_T are those of the WTG transformer.

B. Active and reactive power control

Fig. 1 shows a single WTG grid side converter including its controller. Power transmission through a DR-HVDC link is proportional to the voltage difference between both sides of the DR converter. Moreover, the off-shore ac-grid has a strong capacitive component. Hence, the off-shore ac-grid has a resistive and capacitive characteristic. For this kind of grid, well known P/V Q/ω droops can be used for active and reactive power sharing [8], [24].

The considered active and reactive power controllers are:

$$|V_C^*| = \left(K_{P-droopP} + K_{I-droopP}\frac{T_s}{z-1}\right)(P_{WT}^* - P_{WT}) \quad (4)$$

$$\delta = \left(K_{P-droopQ} + K_{I-droopQ}\frac{T_s}{z-1}\right)(Q_{WT}^* - Q_{WT}) + \omega_0\frac{T_s}{z-1} \quad (5)$$

where $K_{P-droopP}$ and $K_{P-droopQ}$ are the proportional gain for active and reactive power sharing control; $K_{I-droopP}$ is the integral gain for the active power control that ensures optimal power tracking when transmitting power through the DR-HVDC link, and $K_{I-droopQ}$ is the integral gain for the reactive power control to ensure reactive power sharing.

The active and reactive power control droops have been designed following the methodology in [25], [26]. The proposed hierarchical tuning has been carried out independently of the inner voltage control loop. All considered grid-forming voltage control loops will use the same P/V Q/ω droop controller parameters.

C. Baseline Proportional-Resonant voltage controller

The following equation describes the inputs and the output of the controller $\mathbf{K}(z)$.

$$V_{W\alpha\beta}^*(z) = \mathbf{K}(z)\begin{pmatrix} V_{C\alpha\beta}^*(z) - V_{C\alpha\beta}(z) \\ I_{W\alpha\beta}(z) \\ I_{T\alpha\beta}(z) \end{pmatrix} \quad (6)$$

The PR based voltage control (shown in Fig. 2) consists of a cascaded control with an inner current loop and an outer voltage loop. The voltage and current controllers have been designed following the considerations in [27]. For a fair comparison, the PR controller gains have been optimally tuned, following the procedure in Appendix A-C.

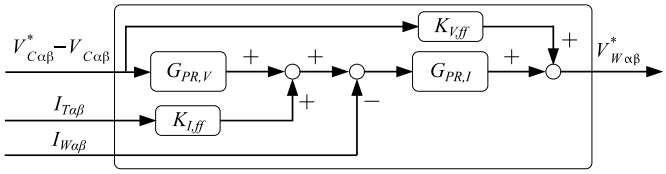

Fig. 2. Block diagram of the PR based controller $K(z)$

D. Problem statement

The main objective of this paper is to propose an $\mathcal{H}_\infty$ based discrete-time controller design methodology for the voltage control of a grid forming controller, considering a wide variation on grid impedance and system structure. The developed controllers are applied to an HVDC DR-connected WPP, where each WTG operates in a variable grid structure (e.g. single WTG islanded operation, parallel WTG in islanded operation with different collector grid structure and different number of connected DR-filters, DR conducting operation and a variable level of load). The proposed controller design methodology considers all the different grid structures during the $\mathcal{H}_\infty$ based discrete-time controller synthesis.

Additionally, the proposed $\mathcal{H}_\infty$ based controller design methodology allows to consider harmonic sources in order to avoid undesired harmonic amplification.

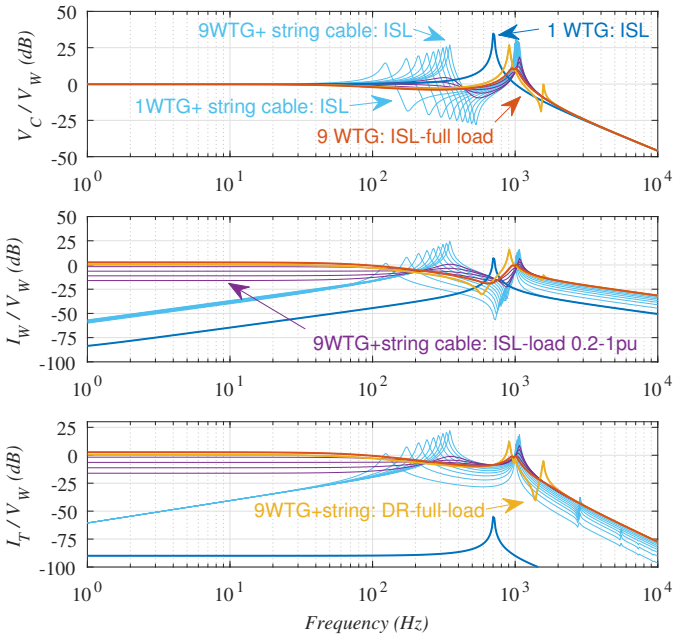

Fig. 3. Frequency response seen from a WTG for each mode of operation blue: one WTG in ISL; dark yellow: DR-connected full load; red: ISL full load, different number of to the string cable in ISL mode (cyan: from 1 WTG to 9 WTGs) and different load levels in ISL load mode (purple: from 0.1pu to 1.0pu)

III. Proposed Voltage Controller Design Methodology

This section describes the proposed $\mathcal{H}_\infty$ controller design methodology, which consists of the following steps: identification of system frequency response considering uncertainty, design of frequency weights, controller synthesis, and finally, performance and robustness analysis.

A. Frequency response for different WPP operating modes

Each WTG will work in different operating modes. In the case of diode rectifier based WPP, three operating modes can be distinguished during normal operation, as discussed in the introduction: ISL, ISL-full load, and DR-connected. The impedance seen by the WTG grid side includes the WTG transformer Z_T in series with the impedance at the PCC (Z_{PCC} in Fig. 4).

To illustrate changes in impedance, Fig. 3 shows the frequency response seen from a WTG for different modes of operation, number of connected WTGs and load levels, corresponding to the black start of the off-shore WPP. At the initial stage, single WTG operating in ISL mode shows a 700 Hz resonance peak corresponding to the Grid Side Converter LC filter (dark blue line in Fig. 3). When the single WTG energises the string cable, and additional resonant peak is produced at 125 Hz while the first peak is moved to 1000 Hz (cyan line of Fig. 3). The connection of the rest of WTGs of the same string (9 WTGs in a string) moves the first resonant peak from 125 Hz to 348 Hz while the higher resonance peak remains around 1000 Hz (group of cyan lines). At this stage, different loads can be connected. The purple lines of the Fig. 3 show the frequency response with all WTGs connected and

loads from 0.1 pu to 1.0 pu. Resonance peaks are attenuated with increasing load util full load operation is reached (red line). Finally, the orange line in Fig. 3 shows the frequency response for a DR-connected WPP transmitting rated power. A resonance around 910 Hz is always presented in this operating mode.

Additionally, the scenario shown in Fig. 1 includes a 12-pulse HVDC DR-connected off-shore WPP, that introduces non linearity because DR behaves as a current source of harmonics 11 and 13 (550Hz and 650Hz considering a 50Hz off-shore network). Hence, controller gain should be limited at these frequencies to avoid performance or stability degradation due to harmonic distortion amplification.

Changes in resonant frequencies and the effects of the DR current harmonics are considered by adequate frequency weights when designing the controllers.

B. $\mathcal{H}_\infty$ controller synthesis and selection of frequency weights

This section discusses the synthesis methodology of the $\mathcal{H}_\infty$ grid forming discrete-time voltage controller (highlighted in green in Fig. 1).

The controller synthesis is carried out following the next steps:

1) Conceptual setting of the problem in generalised plant form.
2) Frequency weight definition (weighted generalised plant).
3) Controller synthesis.
4) Controller order reduction.

1) Generalised plant: In a generic $\mathcal{H}_\infty$ control problem, a generalised plant must be crafted whose inputs are grouped onto (a) setpoints, disturbances, and outputs from uncertainties (assimilated to disturbances), and (b) the manipulated variables (control actions). Conversely, the generalised plant outputs are grouped onto (a) controlled variables and (b) information to controller (usually error signals).

Thus, regarding our particular problem setting, Fig. 4 shows the generalised plant, including output weights W_u, W_i and W_y as control objectives, and the input weights W_{du}, W_{Iw}, W_{It}, W_{Vc} and W_{Vf}.

The nominal plant used for controller design corresponds to the system working in ISL operation (blue frequency response in Fig. 3), because it represents the operation mode with the lowest damping. The selected grid model is discretised using zero-order hold (ZOH) at $2 \cdot f_{PWM}$, as regular asymmetric PWM is used. Additionally, a delay of $1.5 \cdot T_{PWM}$ has been added to the converter voltage input V_{Wi} to consider PWM and calculation delays.

The optimal $\mathcal{H}_\infty$ does not explicitly include uncertainty, and it must be "plugged in" in the generalised plant's weights. Moreover, the desired performance also shall be included as output weights. Therefore, the expected large impedance variations in Z_{PCC} are considered as a disturbance of V_F.

The technical meaning and frequency response of the input and output weights in Fig. 4 are discussed as follows (section III-B2).

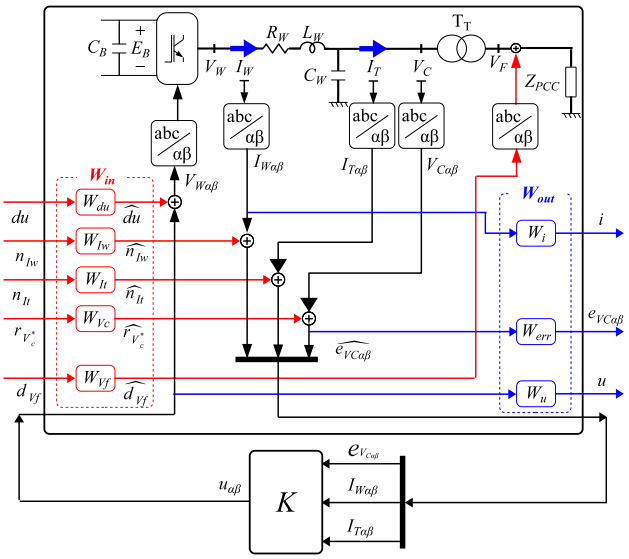

Fig. 4. Control strategies for grid forming WTGs: augmented system with frequency weights

2) Definition of input and output frequency weights: Input weights are used to consider measurement errors and uncertainty, whereas controller performance is defined by means of the output weights.

All the proposed weights are constants or have the form of (7), or (8) below. Constant weights have been used where appropriate not to increase the order of the synthesised $\mathcal{H}_\infty$ controller.

$$G_{weight1} = \frac{K(s+b_0)}{s+a_0} \tag{7}$$

$$G_{weight2} = G_{weight1}\frac{s^2+b_1 s+\omega_0^2}{s^2+a_1 s+\omega_0^2} \tag{8}$$

The purpose of the input weights shown in Fig. 4 is to consider measurement errors and signal uncertainty arising from disturbances or unmodelled dynamics as follows:

- W_{Vc}: this weight defines the frequency range of the reference voltage $r_{V_C^*}$ to be tracked and is a low pass filter with the form of eq. (7). Its low frequency gain is 1.0 which means low frequency references should be tracked. Conversely, a gain of 0.1 is set for frequencies above 200 Hz, so medium and high frequency references are not tracked.
- W_{du}: This weight allows to take into account system delay and converter non-linearities. A value of 0.5 is fixed to consider a possible error of 50% in the system delay (PWM, control calculation and measurements).
- W_{It}: this weight considers measurement noise to the current I_T and is a constant weight. A value of 0.05 is fixed to consider an error of 5% to that measurement.
- W_{Iw}: it is a constant weight of the I_W current measurement. The aim is the same as the weight W_{It}. A value of 0.2 is set to reduce the measurement weight of I_W in the $\mathcal{H}_\infty$ controller.
- W_{Vf}: it is an input weight that takes into account disturbances at V_F. This weight is a constant that should

be high enough to consider all resonance peaks for the different WTG operating modes (ISL, ILS-full load, DR-connected). Its value is set at 50 (34 dB) as per Fig. 3 top graph.

The top trace of Fig. 5 shows the frequency responses of the input weights.

Output weights in Fig. 4 are defined as follows to achieve the desired performance:

- W_u: it is the converter output (V_W) weight and its purpose is limiting the control action V_W at high frequencies (or frequencies within the uncertainty range due to output impedance changes). This weight has the form of eq. (7) and is a high pass filter. Its low frequency gain is set to 0.1 (-20 dB) as the control action V_W can be up to a 10% higher than rated voltage. For frequencies out of the controller bandwidth, the W_u filter gain is reduced to 3.16 (10 dB) to reduce high-frequency oscillations and amplification of DR produced harmonics up to 3.16 times.
- W_i: it is the current (I_w) weight. This weight is a constant. This weight takes into account the multiplicative uncertainty of the I_w current. Its value is set to 0.6 to consider a relatively high uncertainty of 60%, as the variation of I_w is relatively large for different operating modes.
- W_{err}: it is the voltage error e_{Vc} weight and is tuned to minimise the voltage error $e_{V_{C_{\alpha\beta}}}$. The main objective of the voltage controller is for the V_C voltage to follow its 50 Hz reference. This weight has the form of eq. (8), which corresponds to a low pass filter plus a resonant filter of 50 Hz. The low-pass component at high frequencies reduces the closed loop gain at those frequencies where resonances appear during WPP start-up (in cyan in Fig. 3).

The bottom trace of Fig. 5 shows the frequency responses of the output weights. The values for all the weights are listed in Table I.

TABLE I
PARAMETERS OF GENERALISED PLANT WEIGHTS

Weights for $\mathcal{H}_\infty$ controller synthesis
W_{err}: K = 0.079433, b_0 = 10106.4 , a_0 = 577.1, b_1 = 480.6, a_1 = 1, ω_0 = 2·pi·50;
W_u: K = 3, b_0 = 362, a_0 = 10858.6; W_i: K = 0.6;
W_{Vc}: K = 0.1, b_0 = 1111.0, a_0 = 111.1; W_{It}: K = 0.05;
W_{Iw}: K = 0.2; W_{Vf}: K = 50; W_{du}: K = 0.5;

3) $\mathcal{H}_\infty$ Controller synthesis: The $\mathcal{H}_\infty$ controller below has been obtained using the described weights:

$$u_{\alpha\beta} = K_{\mathcal{H}_\infty} \begin{pmatrix} e_{V_{\alpha\beta}} \\ I_{W_{\alpha\beta}} \\ I_{T_{\alpha\beta}} \end{pmatrix} \tag{9}$$

$$K_{\mathcal{H}_\infty} = \begin{pmatrix} K_{\mathcal{H}_\infty,V_C} & K_{\mathcal{H}_\infty,I_W} & K_{\mathcal{H}_\infty,I_T} \end{pmatrix} \tag{10}$$

The resulting three-input controller transfer function matrix $K(z)$ can be split into a voltage error-feedback component $K_{\mathcal{H}_\infty,V_C}$, the converter current component $K_{\mathcal{H}_\infty,I_W}$, and the transformer current-feedback $K_{\mathcal{H}_\infty,I_T}$. The last two elements

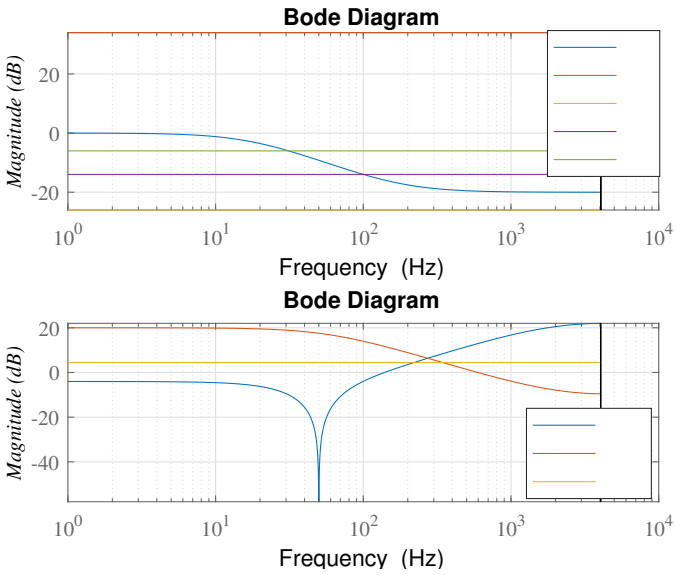

Fig. 5. Weights for $\mathcal{H}_\infty$ design: (a) input weights; (b) output weights

can be considered as virtual impedances as the inputs are currents and their outputs are voltages.

Using the proposed weights, the target closed-loop $\mathcal{H}_\infty$ norm is 0.98, which ensures system stability for the considered uncertainty while achieving the desired performance. As a result, an 11^{th} order controller has been obtained.

4) $\mathcal{H}_\infty$ Controller Order Reduction: The obtained controller order is the sum of plant order and weights order, therefore a high order controller is obtained. Given our performance goal of 1, a method of balanced reduction (Matlab's `balred`) has been applied aiming a keeping the infinity norm of the closed loop weighted plant below 1.02. Applying the balanced reduction method iteratively, the controller has been reduced from order 11 to 6 with negligible performance loss.

C. Summary of the $\mathcal{H}_\infty$ voltage controller design

The proposed methodology to synthesize a voltage $\mathcal{H}_\infty$ based controller for grid forming converters is summarised in Fig. 6. Please note that this is an iterative process whereby the weights are modified to obtain a Normalised Coprime Factor uncertainty margin (robustness margin) larger than 0.25.

The proposed methodology consists of 9 steps. The first part (steps 1 to 4) include modeling the system, discretising the model, identifying system structure changes (it means impedance changes from the WTG point of view), and identifying harmonic current sources to avoid amplifying those frequencies.

The second part (steps 5, 6 and 7) include the following steps: define the input weights considering system uncertainty; then define the output weights considering uncertainty, as well as, the frequency of harmonic current sources and the desired specifications. The controller is synthesized using the Matlab function hinfsyn. Then, the performance of the obtained controller is checked by comparing the infinite norm of the closed loop using the generalized plant with weights. If it is greater than 1, the weights must be redesigned, reducing

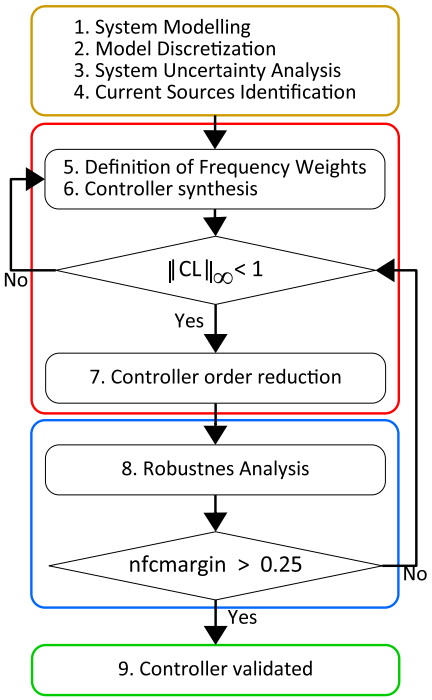

Fig. 6. Grid forming $\mathcal{H}_\infty$ based controller synthesis procedure for DR based WPPs

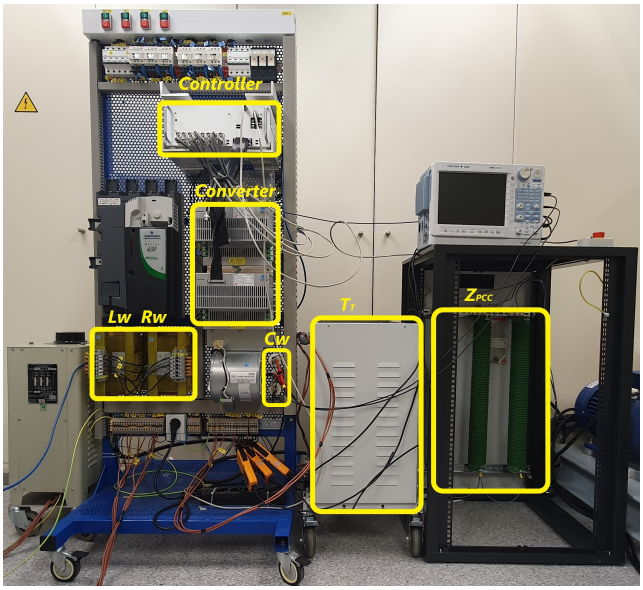

Fig. 7. WTG grid side converter prototype

the performance of the controller or adjusting the input weights to reduce the considered uncertainty. If the achieved infinity norm is less than 1, the order of the controller should be reduced until an infinity norm less than 1.02 is obtained.

The third part includes the robustness analysis of the obtained controller, which is carried out by calculating the coprime factor uncertainty margin for each operating mode. If it is higher than 0.25 in all cases, the robustness of the controller is acceptable as explained below in Section IV-D. Otherwise, the controller shall be re-designed increasing the uncertainty considered for the weights.

After the ninth step, the controller meets the desired NCF margins (i.e., $\approx$ gain and phase margins). Therefore, the designed controller is ready to be validated.

IV. Experimental and Simulation Results

The initial evaluation of the grid forming controller performance is carried out using a reduced power experimental test bench of a single WTG to ensure that system modelling is correct and that the designed $\mathcal{H}_\infty$ design is robust to unmodelled dynamics and non-linearities.

The same procedure is carried out for the baseline PR controller. Power sharing control (droops) are not included for the experimental tests, order to make voltage control loop validation easier.

Finally, the response of both controllers is compared considering the full model of an HVDC DR based off-shore WPP, by means of a detailed EMT simulation.

A. Voltage Control Validation

Fig. 7 shows the reduced power (13.5 kVA) WTG converter prototype, which consists of a grid side converter, an LC filter, a transformer and a resistive load. The values of each parameter are listed in Appendix A-B. The controller is implemented in a TI TMDSCNCD28388D DSP.

Fig. 8 shows the comparison between simulated and experimental results for the baseline PR and the $\mathcal{H}_\infty$ controllers, when a breaker is used to connect the WTG converter transformer and a rated load resistor.

Fig. 8a shows the simulated and experimental results using the baseline PR controller, while Fig. 8b show those with the proposed $\mathcal{H}_\infty$ controller. The match between the simulated and the experimental results is clear, for both the PR and the $\mathcal{H}_\infty$ controllers.

Additionally, the top traces of Fig. 8 clearly show that capacitor voltage recovery to its pre-fault value is about 10 ms faster when using the $\mathcal{H}_\infty$ controller. This is not surprising, as both controllers have been designed with optimal algorithms, and hence the $\mathcal{H}_\infty$ design should give better performance as it has more degrees of freedom that the PR controller. In any case, such a large difference in voltage response is remarkable.

The middle traces show the converter output current (I_w). In this case, the simulated currents follow closely the actual currents up to about t=0.02s. From this point onwards, there is a discrepancy between simulated and experimental currents, due to transformer saturation during connection caused by transformer residual flux. As the model does not consider residual flux, this discrepancy is not unexpected. It is worth noting that the residual flux for the $\mathcal{H}_\infty$ test was larger than that of the PR controller and thus a larger difference between actual and simulated currents for the $\mathcal{H}_\infty$ case. Nevertheless, both controllers keep the capacitor voltage (V_c) close to their reference values despite of residual flux.

Finally, the bottom traces show the error between the reference and actual capacitor voltages. In both cases, the maximum tracking error reaches up to 0.4 p.u. when the transformer is connected. Nevertheless, the $\mathcal{H}_\infty$ controller brings the error close to zero much faster than the PR controller, as

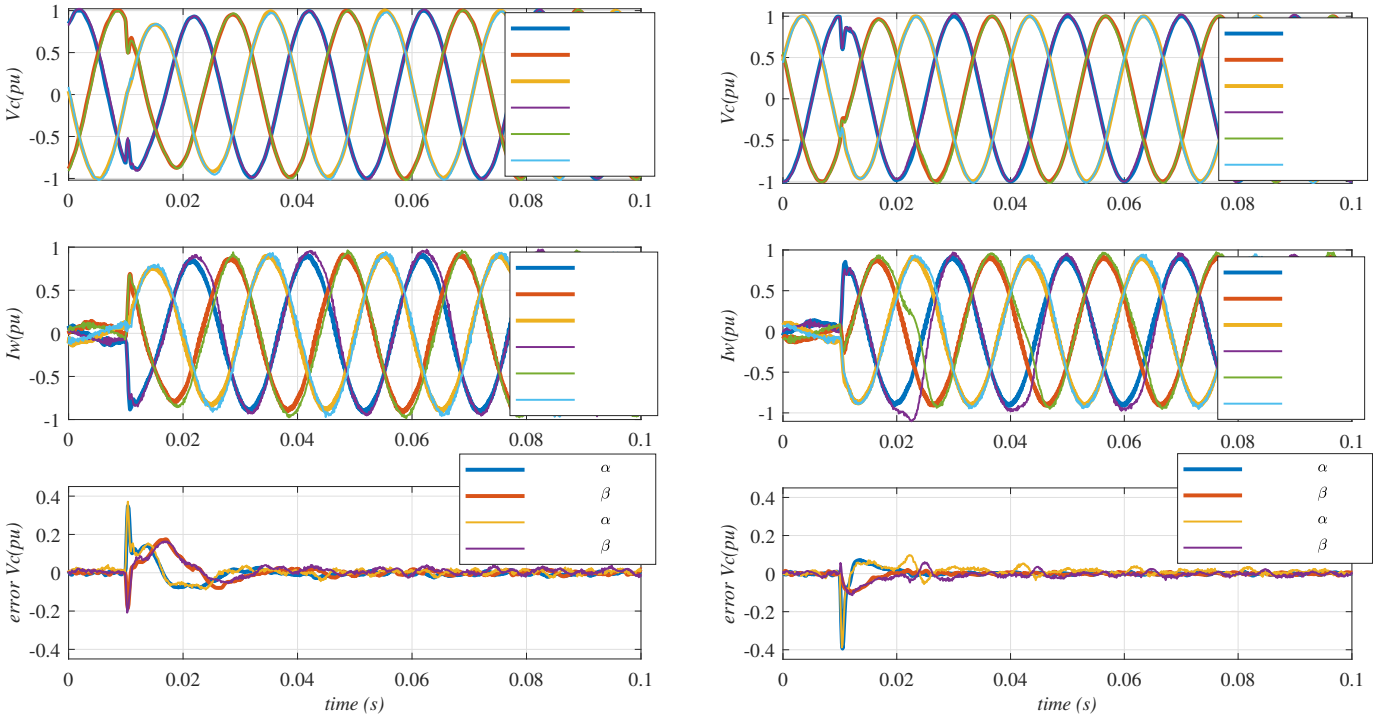

(a) PR based controller (b) $\mathcal{H}_\infty$ based controller

Fig. 8. Comparison between realistic simulation and experimental results: Voltage V_C, current I_W and voltage error $V_C^* - V_C$

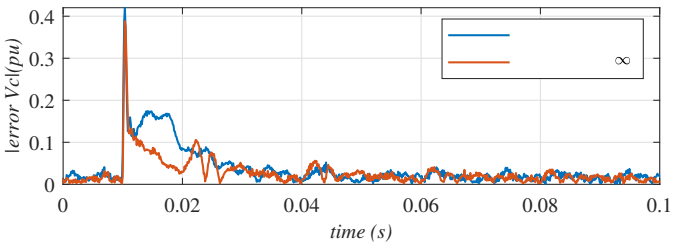

Fig. 9. Comparison of the voltage error magnitude

clearly seen in Fig. 9.

The conclusions from the experimental validation of a single wind turbine converter with full load transformer energisation are that the simulation models are a faithful representation of the experimental system, that both grid-forming controllers show good load rejection performance and that the $\mathcal{H}_\infty$ provides a clearly better dynamic response than the PR controller.

B. HVDC Diode rectifier-connected WPP

Testing on a single or reduced number of experimental prototypes clearly does not consider the actual system complexity. Therefore, in this section, the experimentally validated controllers are used for the detailed EMT simulation of the system described in section II. Fig. 10 shows the simulation results of the complete system considering the optimized PR based controller and the $\mathcal{H}_\infty$ controller.

Initially, the grid forming WPP starts operating in ISL mode. The energisation sequence is omitted for clarity. At $t = 0.1$s and $t = 0.2$s, two Diode Rectifier filter banks are connected consecutively. At $t = 0.5$s, the active power reference of all the WTGs changes from 0 to 0.2 pu. Therefore, off-shore grid voltage increases to 0.92 pu and, hence, the HVDC Diode Rectifier is conducting from this point onwards. At $t = 1$s, the active power reference of WPP_1 is set to 1 pu, at $t = 1.5$s WPP_2 active power reference is set to 0.8 pu and, finally, at $t = 2$s, the active power reference of WPP_3 is set to 0.6 pu. Such large step changes are not realistic in practice, but allow for a better illustration of the behaviour of the different controllers. In both cases, top-level $P - V$ and $Q - \omega$ droop controllers (4) (5) are exactly the same (values included in Table II).

Fig. 10a shows the results obtained with the optimally tuned PR controller, whereas Fig. 10a shows those using the proposed $\mathcal{H}_\infty$ controller.

From top to bottom, the top graph of Fig. 10 shows the WTG capacitor voltages (V_c) and their references, the second graph shows the wind turbine current magnitude (I_W), the third and fourth graphs show the WTG active (P_{WT}) and reactive powers (Q_{WT}); and the fifth graph shows the frequency at the Point of Common Coupling (PCC) of each off-shore WPP.

The dynamic response with both controllers is very similar, as the main system dynamics are dominated by the outer active and reactive power loops in Fig. 1. However, the PR based controller is slightly slower and hence takes a little more time to arrive to the steady-state value. Moreover, the actual capacitor voltage (V_C) tracks its reference with better dynamics when using the $\mathcal{H}_\infty$ controller. Additionally, the PR-controller shows a relatively poorly damped high frequency ripple. The coupling between the active power response of

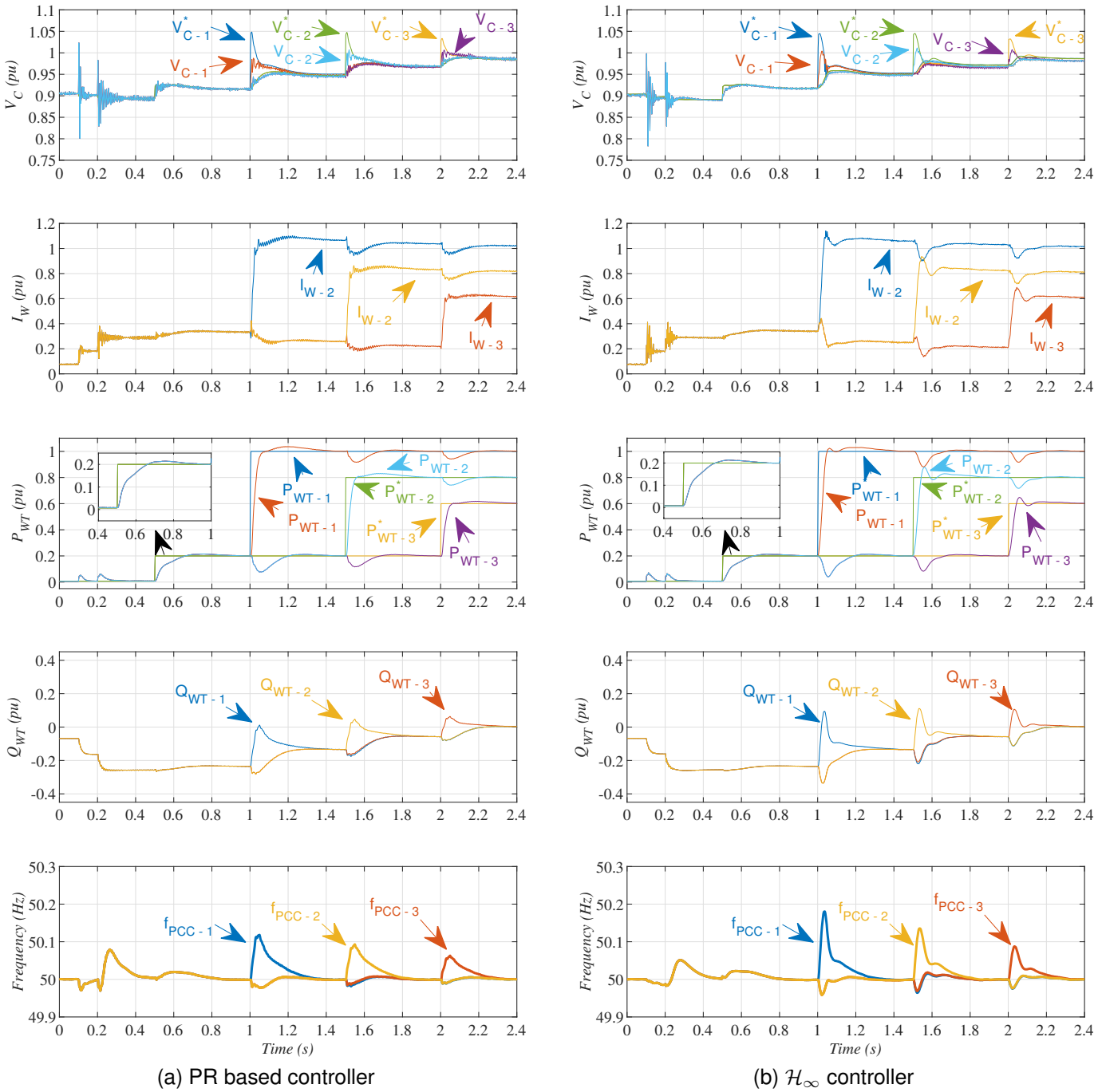

(a) PR based controller (b) $\mathcal{H}_\infty$ controller

Fig. 10. Detailed EMT simulation of the complete system Off-shore Wind Power Plant and DRU-HVDC link: Connection of rectifier filter banks in ISL mode and transition to DR-connected mode with active power steps of each cluster of WTGs (the figure shows the signals of just one WTG per cluster of WTGs)

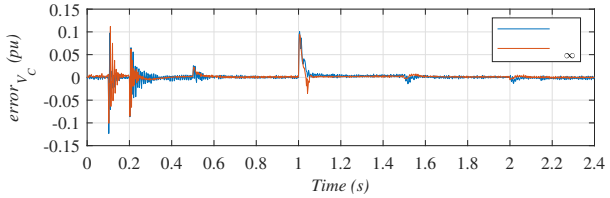

Fig. 11. Voltage error magnitude comparison of the off-shore WPP detailed simulation

each off-shore WPP is similar in both cases.

Note that WPP_1 current (I_{W1}) is slightly larger than unity, corresponding to a power factor of 0.95, well within the WTG capabilities.

To better compare the different behaviour of both controllers, Fig. 11 shows the voltage error ($V_C^* - V_C$) for the PR and $\mathcal{H}_\infty$ controllers. In this figure, the better damping of high frequency ripple provided by the $\mathcal{H}_\infty$ controller is clearly shown.

To assess the influence of the outer $P - V$ and $Q - \omega$ droops, the bandwidth of the outer controllers (4), (5) is

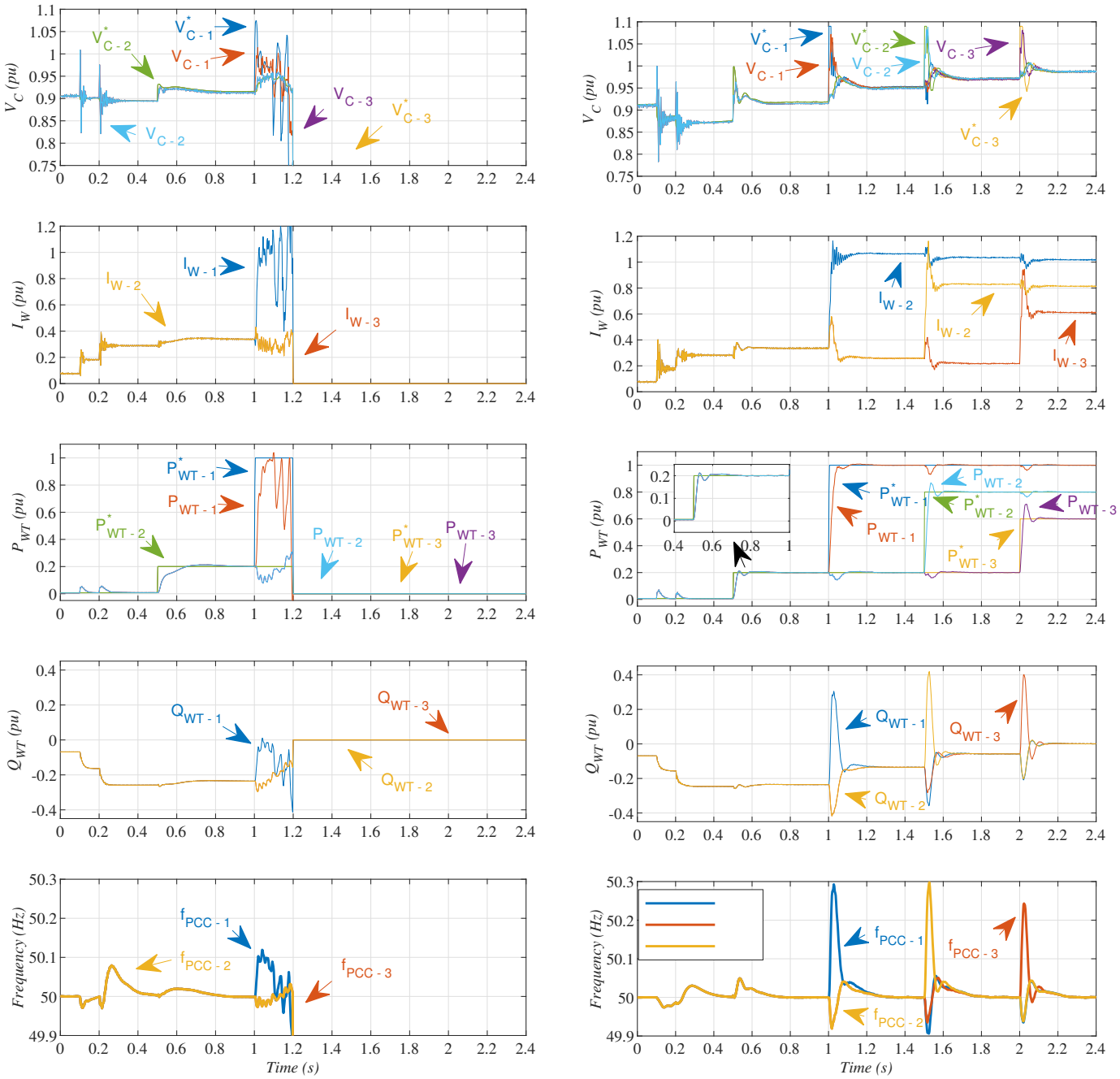

(a) PR based controller (b) $\mathcal{H}_\infty$ controller

Fig. 12. Detailed EMT simulation of the complete system Off-shore Wind Power Plant and DRU-HVDC link: Connection of rectifier filter banks in ISL mode and transition to DR-connected mode with active power steps of each cluster of WTGs (the figure shows the signals of just one WTG per cluster of WTGs)

TABLE II
DROOP CONTROL PARAMETERS

Param.	Init. (PR - $\mathcal{H}_\infty$)	PR unstable	High Perf. ($\mathcal{H}_\infty$)
$K_{P-droopP}$	0.15	0.17	0.4
$K_{I-droopP}$	3.25	3.25	11.7
$K_{P-droopQ}$	0.2	0.2	0.2
$K_{I-droopQ}$	0.5	0.5	0.5

increased (see Tab. II). Fig. 12.a shows that a small increase on the $K_{P-droopP}$ from 0.15 to 0.17 leads to an unstable system when P_{WT-1} reference is increased, leading to system tripping at $t = 1.2s$.

On the other hand, Fig. 12.b shows the response of the system with a $\mathcal{H}_\infty$ controllers considering a higher bandwidth droop controller ($K_{P-droopP} = 0.4$, $K_{I-droopP} = 11.7$). The active power P_{WT} reaches its steady state value in 100 ms with the $\mathcal{H}_\infty$ controller and the high bandwidth droop, while using the previous droop controller it takes about 300 ms. Clearly, the better robustness characteristics of the proposed controller allows for more aggressive outer loop tuning, with much improved active power response and reduced transient cross-coupling. Obviously, improved dynamics are achieved at

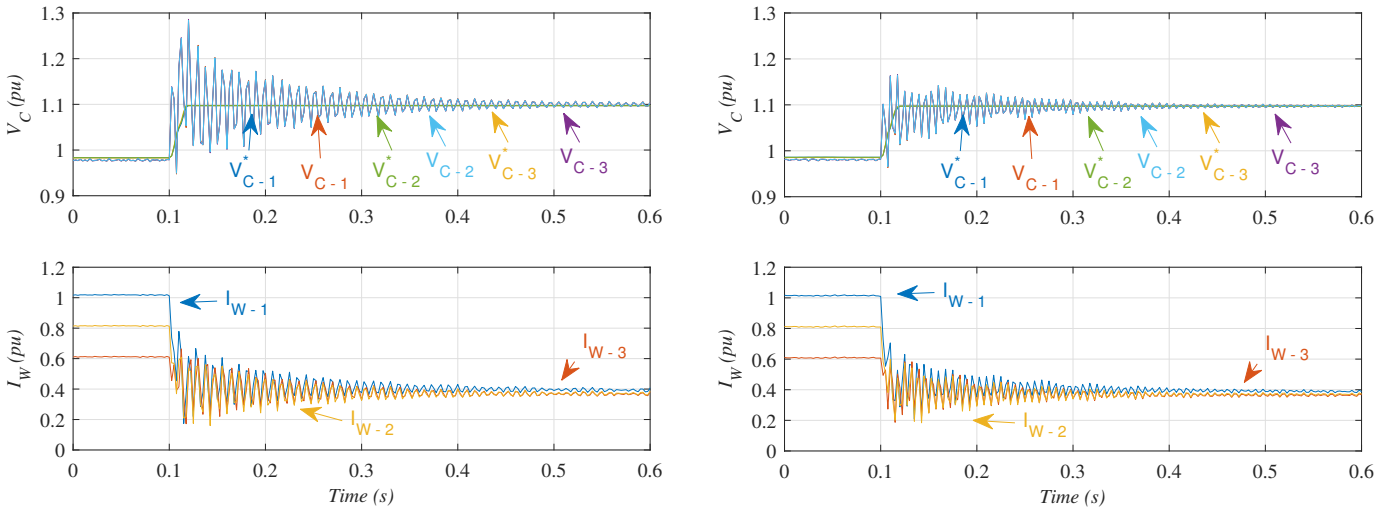

(a) PR based controller (b) $\mathcal{H}_\infty$ controller

Fig. 13. Detailed EMT simulation of the complete system Off-shore Wind Power Plant and DRU-HVDC link: HVDC Diode rectifier trip during power transmission(the figure shows the signals of just one WTG per cluster of WTGs)

the expense of larger control actions and transient frequency deviation.

As with the previous example, Fig. 12 considers active power step changes, which would be unrealistic in a practical case, but are used in order to illustrate the dynamic performance of the proposed solution.

C. Trip of the HVDC Diode rectifier station

The trip of the HVDC DR station has been studied to test the resilience of both controllers. Fig. 13 shows the behaviour of voltages and currents during the DR trip. The voltage V_C rises up to its limit (1.1 pu) in both cases as expected as the droop controllers increase the voltage reference to its maximum value as they try to correct the active power error. The voltage ripple during the disconnection transient and in steady state are substantially lower when using the $\mathcal{H}_\infty$ controller. That is the expected behaviour as $\mathcal{H}_\infty$ controller synthesis allows limiting the control action at specific frequencies (high frequencies in our case). Note that the voltage ripple corresponds to the largest resonance of the off-shore ac grid (around 1 kHz in Fig. 3), which is much more damped with the $\mathcal{H}_\infty$ controller. Again, the $\mathcal{H}_\infty$ voltage control is faster as it was found out if Section IV.

The final value of I_W is around 0.4 pu as now the WTGs must absorb the reactive power produced by the DR filters when there is no power transmission through the HVDC DR.

D. Closed-Loop Robustness Analysis

This section includes the closed-loop robustness analysis for both considered controllers. The robustness analysis is performed by means of the Normalised Coprime Factor (NCF) uncentainty margin. The NCF uncertainty margin [13] of a plant–controller pair can be used for an *a posteriori* assessment of the overall level of robustness of the designs to generic unstructured uncertainty (good NCF uncertainty entails good robustness to additive, multiplicative, additive inverse and multiplicative inverse unstructured uncertainties).

There are two interpretations of this robustness margin:

- first, computing the NCF margin of the nominal design and checking that the other operating modes' associated models are within the NCF uncertainty bound;
- alternatively, computing the NCF margin of the designed controller at the various operation points to see how the controller would tolerate additional unmodelled errors (i.e., impedance/load variations not considered in our set of three representative WTG conditions).

Achieving a good NCF margin entails, in a SISO case, good 'classical' robustness margins. Indeed, if b is the NCF robustness margin of a given plant–controller pair, then [28]:

$$GM(dB) >= 20 * log10((1+b)/(1-b)) \quad (11)$$

$$PM >= 2 * arcsin(b) \quad (12)$$

where GM and PM stand for the well-known gain and phase margins. Usual rules-of-thumb in robust control is aiming for a NCF margin of 0.25 or 0.3, if possible, being in this way in tune with classical GM/PM goals. Indeed, for instance, a NCF margin of 0.25 corresponds with a gain margin of at least 4.4 dB and a phase margin of at least 29 degrees.

There are three operating modes for WTGs in a diode rectifier based WPP (ISL, ISL-full load, and DR-connected). The robustness of the obtained controllers has been obtained by calculating the NCF uncertainty margin for WTGs working in each operating mode. Table III shows the results. The robustness achieved using the $\mathcal{H}_\infty$ based controller is better than that obtained by the PR-based controller for all operating modes.

TABLE III
NORMALISED COPRIME FACTOR UNCERTAINTY MARGIN.

nfc margin	PR	$\mathcal{H}_\infty$
Islanded no-load	0.22	0.26
Islanded rated load	0.20	0.29
Grid connected (DRU)	0.19	0.30

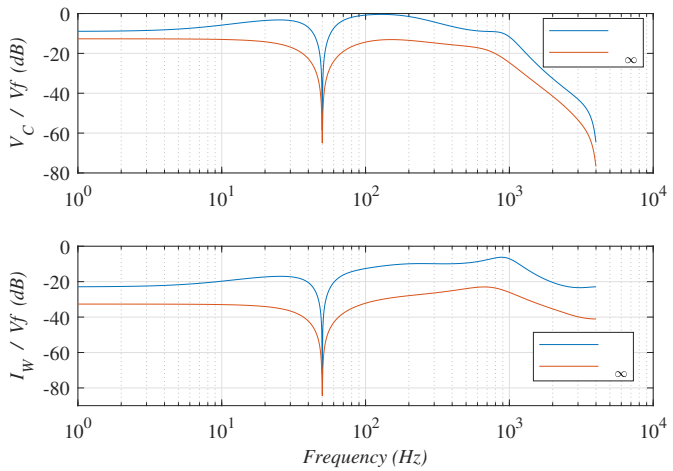

Fig. 14. Bode diagram that shows the disturbance rejection of the close loop control using each controller (PR and $\mathcal{H}_\infty$)

E. Harmonic Analysis

A harmonic analysis has been carried out on the 12-pulse diode rectifier characteristic harmonics (11^{th} and 13^{th}). Table IV shows that both voltage and current harmonic amplitudes are lower using the $\mathcal{H}_\infty$ based controller, thus achieving better harmonic rejection and allowing for harmonic filter reduction. This is the expected behaviour as the $\mathcal{H}_\infty$ based controller has a better voltage and current rejection to V_f harmonics, as clearly shown in Fig. 14.

TABLE IV
EMT SIMULATION. VOLTAGE AND CURRENT HARMONIC COMPONENTS

harmonic	**Voltage (%)**		**Current (%)**	
	PR	$\mathcal{H}_\infty$	PR	$\mathcal{H}_\infty$
11^{th}	0.38	0.29	0.12	0.02
13^{th}	0.42	0.38	0.20	0.10

V. CONCLUSIONS

This paper presents a voltage controller design methodology based on $\mathcal{H}_\infty$ techniques for the voltage control of grid forming converters. The proposed methodology is carried out in the stationary $\alpha - \beta$ frame of reference, which requires achieving a controller with resonant behaviour.

This paper included guidelines on selecting the input and output weights for controller design considering the frequency ranges in which the system is uncertain and those frequencies with characteristic harmonics to be minimised. The obtained controllers show better performance, robustness and harmonic rejection than achieved using a classical control structure based on an optimally tuned PR-controller.

The proposed controller and the baseline PR controller have been compared using three different tools, namely using a scaled down experimental prototype of a single WTG, a real-time Control-Software-in-the-Loop simulation validated against the experimental protype and, finally a detailed simulation considering a system of appropriate complexity.

The real-time simulator results closely match those obtained with the experimental prototype, hence validating the model that will be used for the large system simulation. Moreover, the experimental results and the real-time simulation show clearly that the proposed voltage controller is clearly faster than the optimally tuned PR-controller.

Finally, the detailed simulation of the realistic off-shore WPP with the HVDC DR link shows that the $\mathcal{H}_\infty$ controller allows robust operation during the complete system energisation, with widely changing system impedance and achieves better dynamic performance and harmonic rejection that its PR-controller counterpart.

Regarding robustness, it has been shown that the $\mathcal{H}_\infty$ controller has a better coprime factor uncertainty margin than the optimally tuned PR voltage controller for all the operating modes (ISL, ISL-ful load, and DR-connected), and hence, better gain and phase margins. Additionally, by using the $\mathcal{H}_\infty$ controller it is possible to improve the droop based outer loop control bandwidth to values that would render a PR voltage control solution unstable. The use of a marginally more complex technique for the controller design allowed to consider the operating modes during controller design, leading to a better dynamic performance and a more robust controller.

APPENDIX A

A. Calculation of system impedance (Z_{PCC}) for each operating mode

The equivalent impedance Z_{PCC} includes the off-shore array cable using PI-models, the DR filter bank impedance $Z_{acfilters}$ and the DR transformer impedance. The dynamics of the DR filter bank according to [29] are:

$$V_F = V_{Ca1} + V_{Ca2} + L_a \frac{dI_{La}}{dt} + R_{a1} I_{La} \tag{13}$$

$$V_F = V_{Cb} + L_b \frac{dI_{Lb}}{dt} \tag{14}$$

$$I_{ZFa} = I_{Ca1} + I_{Cb} \tag{15}$$

$$I_{Ca1} = C_{a1} \frac{dV_{Ca1}}{dt} \tag{16}$$

$$I_{Cb} = C_b \frac{dV_{Cb}}{dt} \tag{17}$$

$$V_{Ca2} + L_a \frac{dI_{La}}{dt} + R_{a1} I_{La} = (I_{Ca1} - I_{La})\, R_{a2} \tag{18}$$

$$L_b \frac{dI_{Lb}}{dt} = (I_{Cb} - I_{Lb})\, R_b \tag{19}$$

$$I_{La} = C_{a2} \frac{dV_{Ca2}}{dt} \tag{20}$$

The dynamics of the DR impedance Z_{DR} is as follows:

$$V_F = L_{DR} \frac{dI_{LDR}}{dt} + V_{DR} \tag{21}$$

TABLE V
SYSTEM PARAMETERS

Wind Turbines
Grid-side converter: 8 MW, 1.2 kVcc, 690 Vac, 50 Hz
Grid-side filter: $R_T = 476.1\ \mu\Omega$, $L = 18.94\ \mu$H, $C = 2674\ \mu$F
Transformer: 9.2 MVA, 0.69/66 kV, $R_W = 0.004$ pu, $X_W = 0.1$ pu, Saturable
PWM converter frequency: $f_{PWM} = 4050\ Hz$
Off-shore ac-grid
WTG to WTG distance: 2 km
WTG to ring-bus distance: 4 km
Distance between platforms: 10 km
String cable sections: C = 150 mm^2, B = 185 mm^2, A = 400 mm^2
String with 8 WTGs: C-C-B-B-B-B-B-A
String with 9 WTGs: C-C-B-B-B-B-B-A-A
DRU Platform
Filter and compensation filter bank according to [29]
Transformer: 215 MVA, 66/43/43 kV, $R_{TR} = 0.004$ pu, $X_{TR} = 0.27$ pu
dc-smoothing reactor: 66.67 mH
On-shore full-bridge MMC
MMC: 1200 MW, $\pm$320 kVcc, 370 kVac, 50 Hz
MMC arm reactor: 50 mH
MMC reactor: 1.25 mH, 1 Ω
Transformer: 1400 MVA, 370/230 kV, $X_V = 0.1$ pu

TABLE VI
SMALL POWER PROTOTYPE PARAMETERS

Wind Turbines
Grid-side converter: 13.5 kW, 400 Vac, 50 Hz
Grid-side filter: $R_T = 0.05\ m\Omega$, $L = 3\ m$H, $C = 12\ \mu$F
Transformer: 15 KVA, 400/400 V, $R_W = 0.004$ pu, $X_W = 0.06$ pu,
PWM converter frequency: $f_{PWM} = 4050\ Hz$

B. System parameters

Table V shows the parameters values components of the WPPs connected to the on-shore ac-grid via a diode-based HVDC link.

Table VI shows the parameters component values of the WTG prototype.

C. PR based voltage controller tuning

The equation that describes the PR based voltage controller $\mathbf{K}(s)$ that is shown in Fig. 2 is:

$$K_{PR} = \begin{bmatrix} K_{V,ff} - G_{PR,V} \cdot G_{PR,I} & -G_{PR,I} & K_{I,ff} \cdot G_{PR,I} \end{bmatrix} \tag{22}$$

where $G_{PR,V}$ and $G_{PR,V}$ are

$$G_{PR,V}(s) = K_{P,V} + \frac{K_{R,V} \cdot s}{s^2 + \omega_0^2} \tag{23}$$

$$G_{PR,I}(s) = K_{P,I} + \frac{K_{R,I} \cdot s}{s^2 + \omega_0^2} \tag{24}$$

$K_{V,ff}$ is the voltage feedforward gain and $K_{I,ff}$ is the current feedforward gain.

From (22) and considering the structure of the PR based voltage controller that is shown in Fig. 2, the controller parameters have been obtained optimising the following cost function:

$$J(\Theta) = \sum_{k=0}^{N} error_{Vc}(k)^2 + \sum_{k=0}^{N} error_{Iw}(k)^2 + \sum_{k=0}^{N} r \cdot V_W(k)^2 \tag{25}$$

where Θ includes the following PR parameters and feedforward gains: $\Theta = K_{P,V}, K_{R,V}, K_{P,I}, K_{R,I}, K_{V,ff}, K_{I,ff}$

Table VII shows the values of the parameters obtained for the controller.

TABLE VII
PROPORTIONAL-RESONANT CONTROL PARAMETERS.

Optimally tuned PR controller
$G_{PR,V}$: $K_{P,V}$ = 0.63, $K_{R,V}$ = 189.0; $K_{V,ff} = 0.72$
$G_{PR,I}$: $K_{P,I}$ = 0.243, $K_{R,I}$ = 415.0; $K_{I,ff} = 0.69$

REFERENCES

[1] R. Blasco-Gimenez, S. Añó-Villalba, J. Rodríguez, F. Morant, S. Bernal, Uncontrolled rectifiers for hvdc connection of large off-shore wind farms, in: Power Electronics and Applications, 2009. EPE'09. 13th European Conference on, IEEE, 2009, pp. 1–8.

[2] R. Blasco-Gimenez, S. Añó-Villalba, J. Rodriguez-D'Derlée, S. Bernal-Perez, F. Morant, Diode-based HVdc link for the connection of large offshore wind farms, IEEE Transactions on Energy Conversion 26 (2) (2011) 615–626, 00047. doi:10.1109/TEC.2011.2114886.

[3] S. Bernal-Perez, S. Añó-Villalba, R. Blasco-Gimenez, J. Rodriguez-D'Derlee, Efficiency and fault ride-through performance of a diode-rectifier- and VSC-inverter-based HVDC link for offshore wind farms, IEEE Transactions on Industrial Electronics 60 (6) (2013) 2401–2409. doi:10.1109/TIE.2012.2222855.

[4] P. Menke, New grid access solutions for offshore wind farms, EWEA Off-shore (2015).

[5] S. Seman, R. Zurowski, T. Christ, Investigation of dc converter nonlinear interaction with offshore wind power park system, EWEA Off-shore (2015).

[6] S. Seman, R. Zurowski, C. Taratoris, Interconnection of advanced type 4 WTGs with diode rectifier based HVDC solution and weak AC grids, in: Proceedings of the 14th Wind Integration Workshop, Brussels, Belgium, 20th–22nd Oct, 2015.

[7] R. Blasco-Gimenez, N. Aparicio, S. Añó-Villalba, S. Bernal-Perez, LCC-HVDC connection of offshore wind farms with reduced filter banks, IEEE Transactions on Industrial Electronics 60 (6) (2013) 2372–2380. doi:10.1109/TIE.2012.2227906.

[8] R. Blasco-Gimenez, S. Añó-Villalba, J. Rodríguez-D'Derlée, F. Morant, S. Bernal-Perez, Distributed voltage and frequency control of off-shore wind farms connected with a diode-based HVdc link, IEEE Transactions on Power Electronics 25 (12) (2010) 3095–3105, 00056. doi:10.1109/TPEL.2010.2086491.

[9] L. Yu, R. Li, L. Xu, Distributed PLL-based control of offshore wind turbines connected with diode-rectifier-based HVDC systems, IEEE Transactions on Power Delivery 33 (3) (2018) 1328–1336. doi:10.1109/TPWRD.2017.2772342.

[10] D. Yang, Y. Sun, Analytical small-signal modelling of diode-rectifier based HVDC link based on physical switching actions of diodes, in: 2020 IEEE 21st Workshop on Control and Modeling for Power Electronics (COMPEL), 2020, pp. 1–7. doi:10.1109/COMPEL49091.2020.9265868.

[11] A. Bidadfar, O. Saborío-Romano, N. A. Cutululis, P. E. Sørensen, Control of offshore wind turbines connected to diode-rectifier-based HVdc systems 12 (1) 514–523. doi:10.1109/TSTE.2020.3008606.

[12] Z. Zhang, Y. Tang, Z. Xu, Medium frequency diode rectifier unit based HVDC transmission for offshore wind farm integration 15 (4) (2021) 717–730. doi:10.1049/rpg2.12062.

[13] K. Zhou, J. C. Doyle, Essentials of robust control, Vol. 104, Prentice hall Upper Saddle River, NJ, 1998.

[14] S. Skogestad, I. Postlethwaite, Multivariable feedback control: analysis and design, Vol. 2, Wiley New York, 2007, 07543.
URL http://ieeexplore.ieee.org/iel5/37/4064830/04064853.pdf

[15] R. Teodorescu, M. Liserre, P. Rodriguez, Grid converters for photovoltaic and wind power systems, John Wiley & Sons, 2011.

[16] M. Aten, H. Werner, Robust multivariable control design for HVDC back to back schemes, IEE Proceedings-Generation, Transmission and Distribution 150 (6) (2003) 761–767. doi:10.1049/ip-gtd:20030724.

[17] G. Rigatos, P. Siano, C. Cecati, A new non-linear h-infinity feedback control approach for three-phase voltage source converters, Electric Power Components and Systems 44 (3) (2016) 302–312.

[18] S. Cóbreces, X. Wang, J. Pérez, R. Griñó, F. Blaabjerg, Robust admittance shaping approach to grid current harmonic attenuation and resonance damping, IEEE Transactions on Industry Applications 54 (5) (2018) 5039–5053. doi:10.1109/TIA.2018.2845358.

[19] L. Huang, H. Xin, F. Dörfler, H∞-control of grid-connected converters: Design, objectives and decentralized stability certificates, IEEE Transactions on Smart Grid 11 (5) (2020) 3805–3816. doi:10.1109/TSG.2020.2984946.

[20] M. Chen, D. Zhou, A. Tayyebi, E. Prieto-Araujo, F. Dörfler, F. Blaabjerg, Augmentation of generalized multivariable grid-forming control for power converters with cascaded controllers (2022). arXiv:2202.08639. URL http://arxiv.org/abs/2202.08639

[21] Z. Li, C. Zang, P. Zeng, H. Yu, S. Li, J. Bian, Control of a grid-forming inverter based on sliding-mode and mixed h-2 / h-∞ control, IEEE Transactions on Industrial Electronics 64 (5) (2017) 3862–3872. doi:10.1109/TIE.2016.2636798.

[22] J. Serrano-Delgado, S. Cobreces, E. J. Bueno, M. Rizo, Passivity-based fixed-order h-infinity controller design for grid-forming VSCs, in: 2021 IEEE Applied Power Electronics Conference and Exposition (APEC), 2021, pp. 2459–2466, ISSN: 2470-6647. doi:10.1109/APEC42165.2021.9487406.

[23] J. Martínez-Turégano, S. Añó-Villalba, S. Bernal-Perez, R. Blasco-Gimenez, Aggregation of type-4 large wind farms based on admittance model order reduction, Energies 12 (9) (2019) 1730. doi:10.3390/en12091730.
URL https://www.mdpi.com/1996-1073/12/9/1730

[24] J. M. Guerrero, J. Matas, L. Garcia de Vicuna, M. Castilla, J. Miret, Decentralized control for parallel operation of distributed generation inverters using resistive output impedance, IEEE Transactions on Industrial Electronics 54 (2) (2007) 994–1004, conference Name: IEEE Transactions on Industrial Electronics. doi:10.1109/TIE.2007.892621.

[25] J. M. Guerrero, L. G. d. Vicuna, J. Matas, M. Castilla, J. Miret, Output impedance design of parallel-connected UPS inverters with wireless load-sharing control, IEEE Transactions on industrial electronics 52 (4) (2005) 1126–1135. doi:10.1109/TIE.2005.851634.

[26] W. Yao, M. Chen, J. Matas, J. M. Guerrero, Z. M. Qian, Design and analysis of the droop control method for parallel inverters considering the impact of the complex impedance on the power sharing, IEEE Transactions on Industrial Electronics 58 (2) (2011) 576–588. doi:10.1109/TIE.2010.2046001.

[27] J. C. Vasquez, J. M. Guerrero, M. Savaghebi, J. Eloy-Garcia, R. Teodorescu, Modeling, analysis, and design of stationary-reference-frame droop-controlled parallel three-phase voltage source inverters, IEEE Transactions on Industrial Electronics 60 (4) (2012) 1271–1280. doi:10.1109/TIE.2012.2194951.

[28] K. Glover, G. Vinnicombe, G. Papageorgiou, Guaranteed multi-loop stability margins and the gap metric, in: Proceedings of the 39th IEEE Conference on Decision and Control (Cat. No.00CH37187), Vol. 4, 2000, pp. 4084–4085 vol.4, ISSN: 0191-2216. doi:10.1109/CDC.2000.912354.

[29] M. Szechtman, T. Wess, C. V. Thio, First benchmark model for hvdc control studies, Electra Vol. 135 (Num. 135) (1991) 54–73.